Materials Advances

ROYAL SOCIETY OF CHEMISTRY

PAPER

View Article Online
View Journal | View Issue

Cite this: *Mater. Adv.*, 2025, **6**, 7535

Capacitive behavior of electrodes prepared using tragacanth gum modified at various ratios and temperatures

A. Aliabadi,[a] M. S. Rahmanifar,*[b] B. Sohrabi, *[c] H. Aghaei[a] and K. Zare[a]

In the fields of energy conversion and storage, renewable, affordable, and environmentally benign electrode materials have garnered a lot of interest. Tragacanth gum (TG), a natural polymer, exhibits a high degree of biocompatibility; however, it is still difficult to obtain high conductivity. This study uses a TG carbon precursor and $ZnCl_2$ as an active agent at 600–900 °C for 2 hours under an N_2 atmosphere, which, to the best of our knowledge, is a simple approach for creating porous carbon materials with a high nitrogen content. The resulting TGN-3 sample has a nitrogen content of up to 1.23 weight percent and a high specific surface area of 3595.77 m^2 g^{-1}. Additionally, the N-doped carbon shows good electrochemical properties (with a specific capacitance of 124.78 F g^{-1} in 6 M KOH at a current density of 1 A g^{-1}). Moreover, a TGN-3@Ni composite was prepared from the sustainable carbon source TGN-3 using a straightforward hydrothermal synthesis process. As an electrode material, it demonstrated good electrochemical properties with high rate capability and a specific capacitance of 319.9 F g^{-1} in 6 M KOH at a current density of 5 A g^{-1}. Then, using TGN-3 as the negative electrode, TGN-3@Ni as the positive electrode, and 6 M KOH as the electrolyte solution, an asymmetric supercapacitor (ASC) was fabricated. With a specific capacitance of 40.06 F g^{-1} at 1 A g^{-1} and a high energy density of 16.07 Whkg^{-1} at a power density of 881.07 W kg^{-1}, this supercapacitor demonstrated good electrochemical performance. It also demonstrated exceptional cycle stability, maintaining 96.12% of its initial specific capacitance after 8000 cycles at 5 A g^{-1}. Consequently, these experimental results confirm that porous carbon materials with a high nitrogen content can be prospective electrode materials for supercapacitors.

Received 5th April 2025,
Accepted 28th August 2025

DOI: 10.1039/d5ma00328h

rsc.li/materials-advances

1. Introduction

The abundance, biodegradability and biocompatibility of natural polymers provide them a clear advantage over synthetic ones. Natural gums have gained widespread attention in various sectors of the energy, water, food, environment, biotechnology, and medicine industries due to their accessibility, structural diversity, low cost, and remarkable properties as 'green' bio-based renewable materials.[1] The good qualities of biopolymeric materials, such as their flexibility, lightweight nature, high adsorption capacity, and consistent cycle performance, have led to a recent rise in their popularity for use in supercapacitors. Furthermore, biopolymers are safer, more ecologically friendly, and more recyclable than heavy metals in battery electrodes. For use in energy applications, the inherent properties of these polysaccharides can be modified and improved. Conductive nanoparticles, such as metal nanoparticles (such as silver and gold nanoparticles), carbon-based materials, and metal oxide nanoparticles (such as zinc oxide, titanium dioxide, and iron oxide nanoparticles), can be added to improve electronic conductivity. All in all, biopolymers have become a great source of carbon for creating porous carbon composites.

Astragalus is a shrub in Britain that secretes a natural anionic polymer called tragacanth gum (TG). It is frequently utilized in food additives, thickeners, stabilizers, and hydrogels and possesses excellent biocompatibility, biodegradability, non-toxicity, and acid resistance.[2] This natural gum is a dried exudate gathered from the stems and branches of several *Astragalus* species that are native to Asia's highlands but are most commonly found in the northern parts of Iran. Commercial TGs from various species range significantly in chemical

[a] *Department of Chemistry, Science and Research Branch, Islamic Azad University, Tehran, Iran*
[b] *Faculty of Basic Science, Shahed University, Tehran, Iran. E-mail: rahmanf_m@yahoo.com, rahmanfm@shahed.ac.ir*
[c] *Department of Physical Chemistry, Faculty of Chemistry, Surface Chemistry Research Laboratory, Iran University of Science and Technology, Tehran, 16846-13114, Iran. E-mail: sohrabi_b@yahoo.com, sohrabi_b@iust.ac.ir; Tel: +98-2173228315*

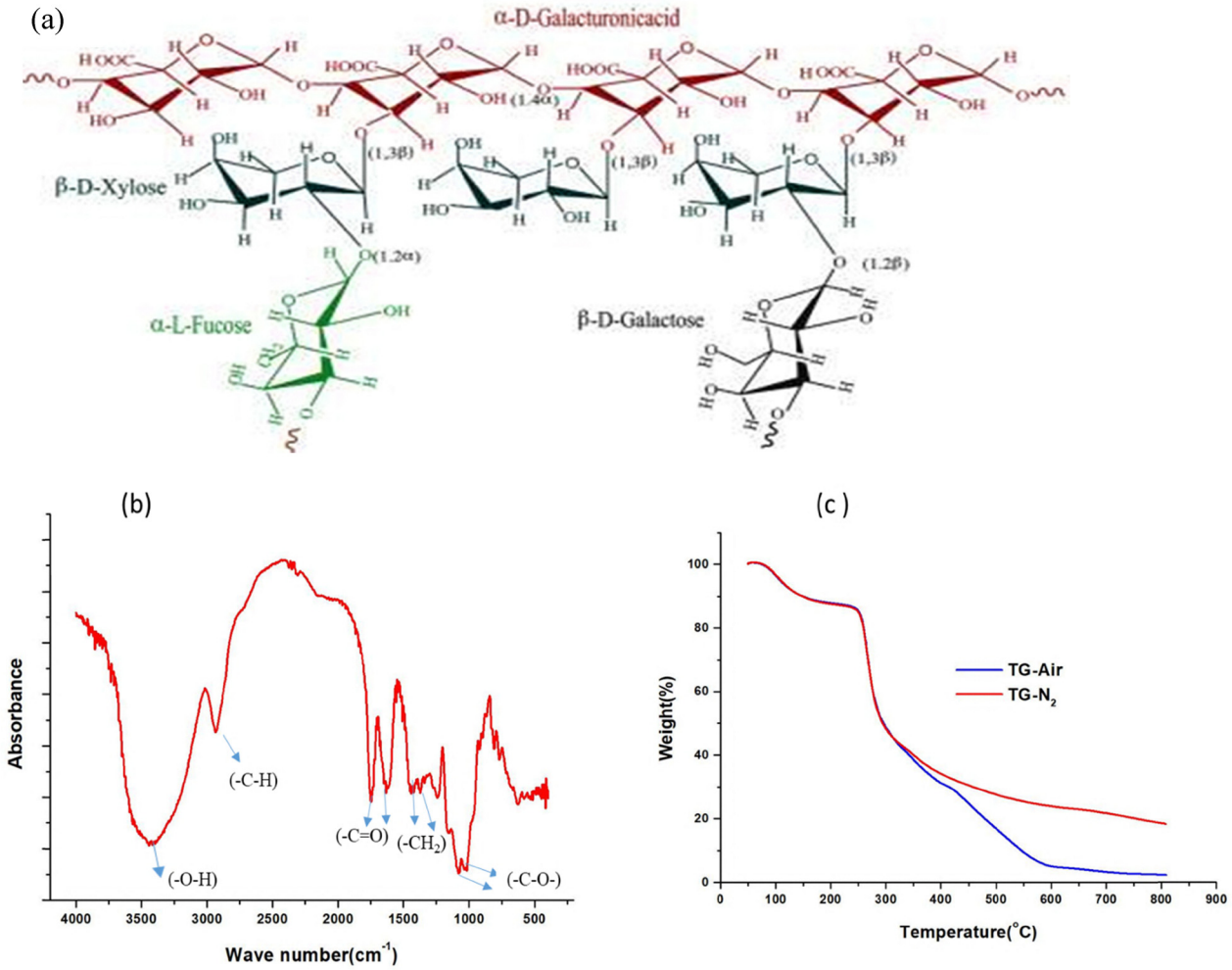

Fig. 1 (a) Structure of the tragacanth gum polysaccharide. Tragacanth gum molecules are composed of sugar residues, including α-D-galacturonic acid, β-D-xylose, α-L-fucose, L-arabinose, galacturonic acid methyl ester, and β-D-galactose.[3] (b) FT-IR spectra of tragacanth gum. (c) Thermal analysis of tragacanth gum powder in the presence of an N_2 atmosphere and air.

composition, including sugar composition, methoxy concentration, and the relative percentage of soluble and insoluble components, owing to seasonal and regional fluctuations. TG is mostly a complex combination of branched acidic heteropolysaccharides that contains D-galacturonic acid. Other sugars generated by hydrolysis include D-galactose, L-fucose (6-deoxy-L-galactose), D-xylose, and L-arabinose. Bassorin (arabinogalactan) appears to be practically neutral, with D-galacturonic acid methyl ester replacing acid units (Fig. 1a). When TG is added to water, the soluble portion, tragacanthin or tragacanthic acid, dissolves to create a viscous colloidal hydrosol, while the insoluble part, bassorin (60–70%), swells to form a gel. An aqueous solution of TG is the most viscous of all natural plant gums, and it is extremely heat stable.[3] Tragacanth gum was employed as a green binder by Scalia *et al.* to fabricate supercapacitors, while a TG/PIL (polymer tragacanth gum and ionic liquid 1-vinyl-3-ethylimidazolium bromide) hydrogel was employed as an electrolyte in more recent studies.[4,5] Furthermore, it has been shown that tragacanth gum is used in the green biosynthesis of various transition metal and metal oxide nanoparticles, including ZnO-NPs,[6] CuO-NPs,[7] AgNPs[8] and Ag@ZnO NPs.[9] Natural biomass types have recently been used as raw materials to create porous carbon materials for supercapacitors.[10]

Activated carbons have been one of the most researched electrode materials in recent decades owing to their inexpensive cost, abundant resources, huge surface area, adjustable porosity, and strong electroconductivity. Activated carbons are advantageous for the quick transfer of electrolyte ions in electrodes and for storing numerous charges on the surface owing to their wide surface area and improved porosity. Physical and chemical activation are the two main types of activation techniques used to prepare activated carbons. As chemical activation agents, KOH, $ZnCl_2$, and H_3PO_4 are typically employed. However, microspores predominate in activated carbons prepared by physical or chemical activation with KOH and H_3PO_4. Additionally, the small pore size severely restricts the supply of electrolyte ions, which

increases the resistance owing to the concentration polarization effect.

The $ZnCl_2$ activation readily produces an adjustable porosity structure from microporous to mesoporous, in contrast to other activation techniques.[11]

As the $ZnCl_2$ impregnation ratio increases, significant dehydration occurs, resulting in increased pore widening and decreased microporosity. In fact, $ZnCl_2$ has hydration and dehydroxylation effects during the activation process, which can release hydrogen and oxygen from the starting material in the form of water vapour and form a porous structure. Furthermore, $ZnCl_2$ is converted into ZnO during the activation process, which can react with carbon to break down its structure and produce many pores.[12,13] According to previous investigations, doping carbon materials with a specific quantity of heteroatoms (such as sulfur, phosphorus, and nitrogen) can enhance their surface stability while increasing a portion of their pseudocapacitance and increasing their overall specific capacity.

To create a novel nitrogen-doped interconnecting porous activated carbon with a high SSA from Tragacanth as a biomass precursor, we developed a practical and effective method. Zinc chloride, a highly effective activator, was used to activate the porous carbon precursor. After doping with heteroatoms, the high-temperature nitriding process was used to swiftly and easily create nitrogen-doped activated carbon with a high SSA. Since nitrogen atom doping improves surface wettability and electrical conductivity, the results indicate that nitrogen-doped activated carbon with high SSA has a higher charge storage capacity.[14] A distinctive nitrogen-doped activated carbon with a high SSA is produced by this easy and effective synthesis procedure, and it has tremendous promise for real-world energy storage applications for high-performance supercapacitors. TG hydrogel's high conductivity is difficult to achieve; thus, in this study, nickel oxide nanoparticles were also employed to alter and enhance the TG polysaccharide's inherent characteristics.[5,14]

2. Experimental section

2.1. Materials

A quantity of high-quality tragacanth (sheet) was purchased from the Tehran market. Other chemicals, such as nickel nitrate hexahydrate ($Ni(NO_3)_2{\cdot}6H_2O$) (98.5%), urea (99%), potassium hydroxide (KOH), hydrochloric acid (HCl), zinc chloride ($ZnCl_2$), ethanol, acetylene black, poly(tetrafluoroethylene), and *N*-methylprolidone (NMP), were purchased from Merck and Sigma-Aldrich Chemical Companies. They were all of analytical purity and were used directly without further purification. Deionized (DI) water was used throughout the experiment.

2.2. Preparation of porous activated carbon material

A total of 2.03 g of Tragacanth powder was slowly dissolved in 200 g of water, and a mechanical stirrer was used to stir the mixture. This mixture was stirred for 3 hours at a speed of 1300 rpm to obtain a homogeneous gel of 1% (w/w). Then, it was freeze-dried to preserve the porous microstructure before and after drying.

Then, the resulting material was ground with a coffee grinder and heated to a temperature of 270 °C in a tube furnace in an N_2 atmosphere at a speed of 3 °C min^{-1} and remained at this temperature for 2 hours until it was pre-carbonized. Then, it was mixed with $ZnCl_2$ in different ratios of 1 : 1, 1 : 2, 1 : 3, and 1 : 4 (TG/$ZnCl_2$ w/w) for activation. Additionally, it was stirred for 6 hours and placed in an ultrasonic bath for 90 min. Ultimately, it was dried in an oven set at 105 °C. The resultant material was then heated to 550 °C at a speed of 5 °C min^{-1} in a tube furnace in an N_2 atmosphere for 90 min. Next, it was heated to 800 °C at a speed of 5 °C min^{-1}, where it stayed for 2 hours until it was carbonized. The samples were carbonized using the same procedure at 600, 700, and 900 °C and were designated as TG_n-*m*. The activation ratios with zinc chloride and temperature are denoted by *n* and *m*, respectively. Finally, the special black powder was washed with a 0.1 M HCl solution to remove inorganic impurities, and it was washed several times with distilled water to reach a pH of 5–7 and then dried in an oven at 105 °C to obtain porous biomass-activated carbon.

2.3. Preparation of porous N-doped-activated carbon material

To prepare N-doped activated carbon (TG_{1-3}-800), urea ($CO(NH_2)_2$) was used as a nitrogen source. The TG_{1-3}-800 and urea samples were uniformly ground and mixed according to mass ratios of 1 : 1, 1 : 2, 1 : 3, and 1 : 4 (TG_{1-3}-800 : urea w/w), and the obtained TGN was named TGN-1, TGN-2, TGN-3, and TGN-4, respectively. Then, they were placed in a tube furnace under an N_2 atmosphere for safety. The temperature was increased to 800 °C at a heating rate of 10 °C min^{-1} and held at a constant temperature of 800 °C for activation for 15 min. The boiling water was used to wash the product and eliminate any extra urea decomposition products to reach a pH of 5–7. Next, the obtained product was dried at 105 °C to obtain porous nitrogen-doped activated carbon.

2.4. Hydrothermal synthesis of TGN-3@Ni composite

To prepare the TGN-3@Ni composite, 30 mg of TGN-3 powder was dissolved in 15 mL of deionized water using an ultrasonic bath with 63.9 mg of $Ni(NO_3)_2{\cdot}6H_2O$. Then, 439.5 mg of urea was swiftly mixed into the solution until it was homogenous.[15]

The suspension was then enclosed in 50 mL Teflon-lined stainless steel autoclaves to undergo a hydrothermal reaction at 180 °C for 16 hours. After cooling the autoclave to room temperature, the black precipitate was centrifuged, washed with distilled water and ethanol, and dried in an oven at 105 °C for 12 hours to produce the precursor TGN-3@Ni. Finally, the precursor was calcined in air at 550 °C for 90 min to produce TGN-3@Ni.

2.5. Characterization

With the support of various techniques, such as scanning electron microscopy (SEM and FE SEM), transmission electron

microscopy (TEM), and energy dispersive X-ray (EDX) mapping, evidence of the internal architecture, external morphology, crystallinity, and chemical composition of hollow structures can be obtained. In this regard, the morphology and structure of the samples were observed by scanning electron microscopy (SEM, Tescan Vega3 and FE-SEM, Tescan MIRA4), EDX (Tescan Vega2) and transmission electron microscopy (TEM, Zeiss Em10). The phase structure of the materials was characterized by X-ray powder diffraction (XRD) equipped with Rigaku Ultima IV. Raman spectra were obtained using a microscopic confocal (532 and 785 nm) Raman spectrometer. Nitrogen sorption isotherms were measured on a surface characterization analyser (Micromeritics ASAP 2020M) at 77 K. The Brunauer–Emmett–Teller (BET) technique was used to obtain the specific surface area, and the Barrett–Joyner–Halenda (BJH) method was used to produce the isotherms, which were then used to calculate pore size distributions. The surface functional groups of the prepared TG sample were detected using Fourier transform infrared spectrometry (FTIR) on a PerkinElmer 1720-X Infrared Spectrometer. Thermogravimetric analysis was performed using a Polymer TG thermal gravimetric analyser (Mettler Toledo 851) at temperatures ranging from ambient to 800 °C in the presence of N_2 atmosphere and air at a heating rate of 10 °C min^{-1}. The surface elemental species of the final products were evaluated using X-ray photoelectron spectroscopy (XPS, Bestec, Ea10). The working electrode was prepared by blending the as-synthesized components, acetylene black and poly (tetrafluoroethylene) in mass ratios of 85%, 10%, and 5%, respectively. The mixture was dispersed in *N*-methyl pyrrolidone (NMP) to form a slurry. This slurry was then pressed onto nickel foam, each with an active mass loading of around 1.0 mg.

Using a three-electrode setup in a 6 M KOH electrolyte solution, an electrochemical test was conducted at room temperature. The Ag/AgCl electrode was used as the reference electrode, the platinum sheet as the counter electrode, and the synthesized materials as the working electrodes in the three-electrode system. Biologic SP-300 electrochemical measurements, such as galvanostatic charge/discharge (GCD), electrochemical impedance spectroscopy (EIS), and cyclic voltammetry (CV), were performed using the kimiestate135 electrochemical workstation. The voltage for the galvanostatic measurement ranged from −1.02 to 0.2 V and from 0 to 0.5 V for TGN-3 and TGN-3@Ni, respectively, while the voltage for the CV test ranged from −1.18 to 0.2 V and from 0 to 0.56 V at various scan rates of 10–200 mV s^{-1}. Electrochemical impedance spectroscopy (EIS) was performed at frequencies ranging from 100 kHz to 0.01 Hz.

2.6. Fabrication of the device

An asymmetric supercapacitor (ASC) was installed with TGN-3@Ni as the positive electrode, TGN-3 as the negative electrode, and 6 M KOH as the electrolyte solution to further explore the potential of the TGN-3@Ni composite in real-world applications.

Based on the charge balance in an ASC ($Q_+ = Q_-$), where Q_+ is the positive electrode charge, Q_- is the negative electrode charge, and $Q = (C \times m \times \Delta V)$, the mass ratio of the two electrode materials was obtained using eqn (1):[16]

$$\frac{m_+}{m_-} = \frac{C_- \times \Delta V_-}{C_+ \times \Delta V_+}, \quad (1)$$

where the specific capacitances of positive and negative electrodes are denoted by C_+ and C_-, respectively; the potential windows of positive and negative electrodes by ΔV_+ and ΔV_-, respectively; and the masses of positive and negative materials by m_+ and m_-, respectively. Based on the equation, the mass ratio of TGN-3@Ni to TGN-3 is about 0.33.

3. Results and discussion

3.1. FT-IR analysis

The chemical makeup and functional groups of tragacanth gum were determined using Fourier transform infrared spectroscopy. Its nature as a polysaccharide is shown by distinctive peaks in the FTIR spectrum (Fig. 1b). In particular, (–O–H) stretching vibrations are responsible for the broad bands at 3274–3492 cm^{-1}, whereas (–C–H) stretching vibrations are responsible for the bands at about 2919–2922 cm^{-1}. Furthermore, bands at 1373–1474 cm^{-1} indicate ($-CH_2$) bending vibrations, while peaks at 1650–1750 cm^{-1} show (–C═O) stretching vibrations. Between 1011 and 1026 cm^{-1}, (–C–O–) stretching vibrations are visible.

3.2. Thermal gravimetric analysis (TGA)

Thermal analysis has been widely used to gain knowledge of the thermal behaviors of agricultural by-products.

According to the TGA curves in (Fig. 1c), TG showed three steps of weight losses of about 12%, 38%, and 25% at around 150 °C, 260 °C, and 420 °C, respectively, which can be attributed to the loss of absorbed water and side groups, such as acid and ester groups. The decomposition of the main chain, and the residual ash weight for pure TG at 600 °C in a controlled nitrogen environment and exposed to air were 23.91% and 4.49%, respectively, and there was no detectable weight loss at higher temperatures. Therefore, this temperature could be the lowest carbonization temperature for the production of activated carbon from TG.

3.3. Scanning electron microscopy (SEM)

To transport electrons and electrolyte ions as well as the electrochemical stability of the electrode materials, the shape of the electrode active material can produce active sites and additional penetration channels. The SEM photos of the synthesized TG_n-*m* electrode material samples reveal that they are made up of tiny, clumped carbon microsphere particles with an uneven exterior and interstitial space, which can lead to electrolyte ion diffusion and transport.

The average diameter of carbon microspheres and the number of internal pores in the synthesised electrode materials can be increased by increasing the temperature during the carbonisation process and increasing the activation ratio with

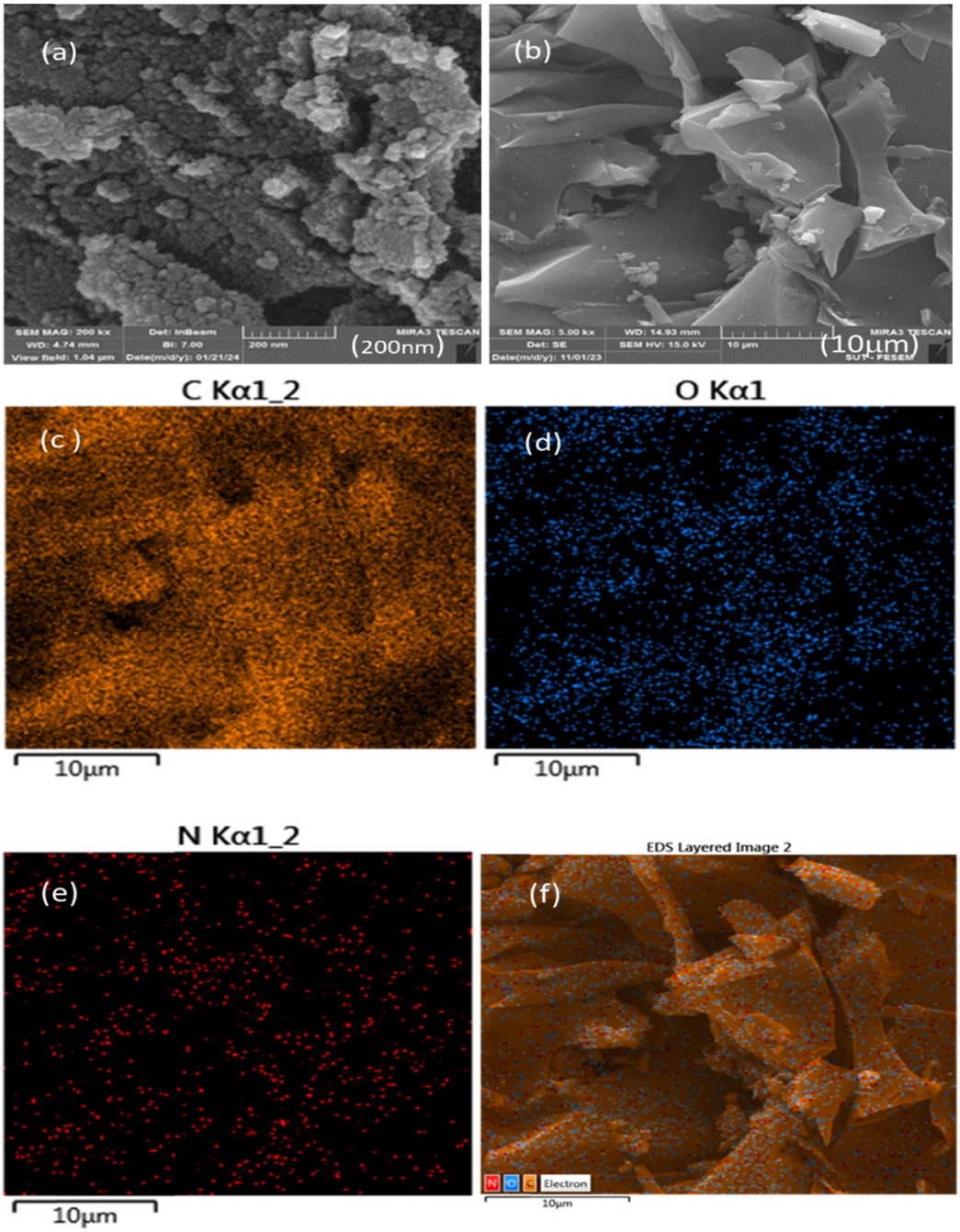

Fig. 2 (a) and (b) FE-SEM images of TGN–3. (c)–(f) Elemental mapping images of TGN–3.

$ZnCl_2$, resulting in a more uniform pore distribution, according to an analysis of the SEM images (Fig. S1). The collapse of large pores on the material's surface owing to excessive $ZnCl_2$ addition and temperature causes the creation of abnormally large pores. The material's initial three-dimensional pore structure is upset as a result of the smaller pores adhering to one another.

The increased number of defects in the carbon skeleton of the nitrogen-doped electrode active material results in more active sites for storing charge and the expansion of the carbon microsphere structure, which has an average diameter of around 20.96 nm and increases the electrode active material's contact area with the electrolyte (Fig. 2a and b FESEM images of the optimized electrode material TGN-3).

A large variety of chemical components, as well as the distribution and dispersion of those elements inside the sample, can be found using EDX analysis. The elemental mapping pictures of TGN-3 are displayed in Fig. 2c–f. These pictures verify that C, O, and N are present in the TGN-3 electrode's active material. Additionally, these pictures demonstrate how evenly dispersed the O and N atoms are in the bulk carbon matrix.

One of the most popular microscopic studies for examining and studying the morphology and microstructure of materials

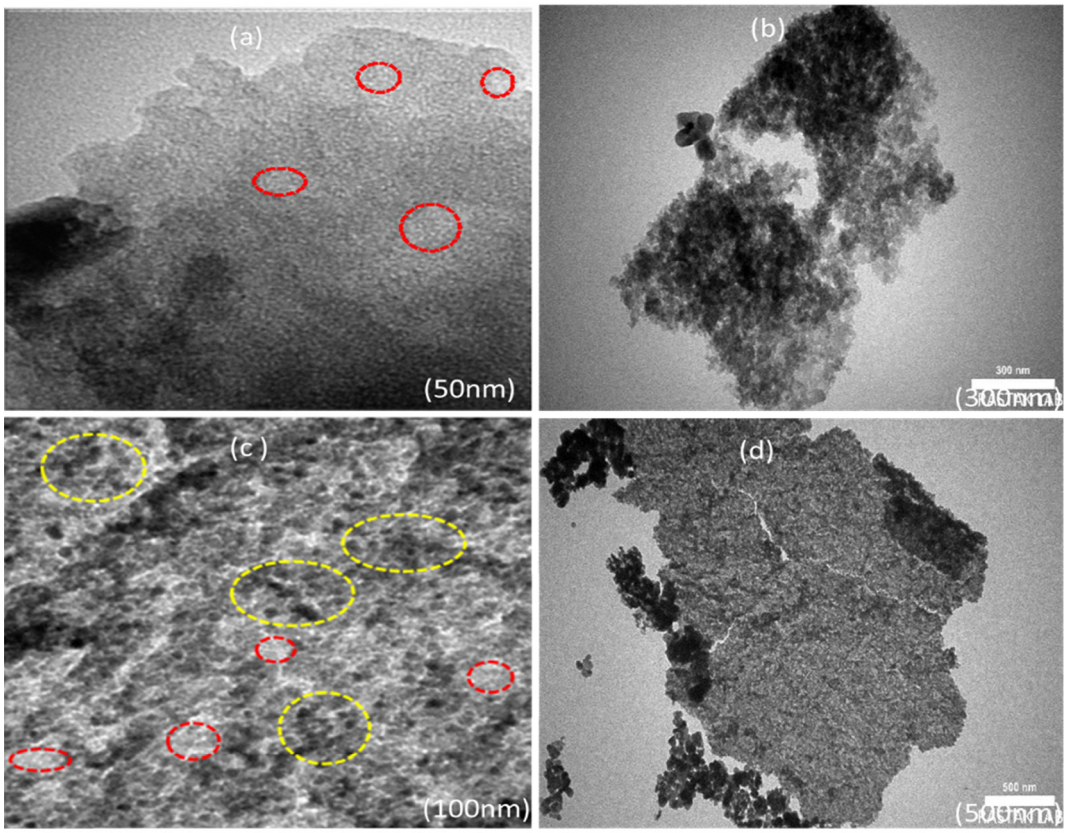

Fig. 3 (a) and (b) TEM (HR-TEM) micrographs of tragacanth gum–derived carbon TGN-3. (c) and (d) TEM micrographs of the TGN-3@Ni composite.

is TEM. High-resolution TEM pictures of the TGN-3 sample are displayed in Fig. 3a and b. The presence of uniformly distributed white spots throughout the sample (shown by red dashed circles in Fig. 3a) indicates the presence of highly developed amorphous porous features. This feature is confirmed by the XRD results and is caused by the release of gaseous contents during the carbon activation process and nitrogen doping in the TG N-3 electrode's active material,[17,18]

To learn more about the microstructure of the TGN-3@Ni composite, TEM research was conducted. The nickel oxide nanoparticles in the TGN-3@Ni composite are uniformly embedded in the TGN-3 carbon matrix, as demonstrated by the high-resolution TEM images (Fig. 3c and d). Their monodisperse nature is evident in the figure, and the yellow and red circles in Fig. 3c represent nickel oxide nanoparticles and carbon thin layers, respectively. Although the carbon layers are anticipated to enhance electrical conductivity and the metal oxide nanoparticles offer more active sites, the pores in the composite may result in an increase in the specific surface area. Consequently, a sizable electroactive surface with excellent electrochemical performance is produced without any appreciable NiO nanoparticle aggregation.[19,20]

3.4. BET specific surface area and pore size analysis

BET analysis was carried out to determine the precise surface area, diameter, volume, and pore size distribution of the synthesized electrode active materials. Table 1 provides a summary of the BET surface area, pore size distribution, and pore volume parameters of the porous carbon in the samples of synthetic electrode active materials. The BET method was used to obtain the total surface area in Table 1, the *t*-plot method was used to determine the micropore surface area and volume, and the Barrett–Joyner–Halenda (BJH) method was used to determine the total pore volume and average pore diameter based on the desorption.

Since the use of porous carbon materials requires a pore size distribution, nitrogen adsorption and desorption experiments were used to assess the specific surface area and pore structure of the samples.

Micropores, mesopores, or macropores can coexist in the TG_{1-3}-800, as shown in Fig. 4a, according to a mixed I/IV type isotherm with very steep uptakes at low relative pressure (P/P_0) and a typical hysteresis loop extending P/P_0 from 0.4 to 1.0.[21]

The TGN-3 sample exhibits adsorption behavior that is more akin to the type I adsorption curve; the micropore filling effect causes the adsorption content to increase rapidly in the low relative range, followed by multilayer sorption and capillary condensation at a higher pressure. Furthermore, the presence of macropores is indicated by the increasing trend of isotherm tails at relative pressures around unity. It is evident from this that TGN-3 has a considerable number of macropores, mesopores, and micropores.[22]

A greater specific surface area is attained as a result of the production of more pores, as illustrated in the flat plateau of

Table 1 Total surface area calculated using the BET method. Micro pore surface area and volume calculated using the *t*-plot method. Total pore volume calculated at P/P_0 = 0.97. Average pore diameter calculated from BJH desorption

Sample name	BET surface area $m^2\ g^{-1}$	*t*-plot external surface area $m^2\ g^{-1}$	*t*-plot micropore area $m^2\ g^{-1}$	*t*-plot micropore volume $cm^3\ g^{-1}$	BJH desorption average pore with (nm)	Total pore volume at P/P_0 = 0.97 $cm^3\ g^{-1}$	V_{mi}/V_t (%)
TG_{1-1}-800	890.08	141.89	748.19	0.348	3.532	0.442	78.73
TG_{1-2}-800	1702.12	571.00	1131.11	0.519	5.015	1.123	46.21
TG_{1-3}-800	4302.83	2776.88	1525.95	0.664	4.300	2.1	31.61
TGN-3	3595.77	2850.29	745.48	0.293	3.928	1.67	17.54
TG_{1-3}-600	2362.25	1617.98	744.26	0.308	2.632	1.186	25.96
TG_{1-1}-700	2236.99	1621.14	615.84	0.252	2.673	1.156	21.79
TG_{1-3}-900	1931.77	1645.10	286.67	0.110	3.197	1.488	7.39
TG_{1-4}-800	4760.24	8025.33	—	-2.05	4.05	5.12	—

the isotherms in Fig. 4a, moving to a higher position when the activation temperatures increase from 600 °C to 800 °C.[23]

For the process of charge storage, a large specific surface area (SSA) can offer a large number of electrochemically active sites. Shortening the electrolyte ion diffusion route can be achieved by increasing the SSA owing to the porous structure and exposition of the interior material for improved contact with the electrolyte. Thus, SSA and porous structure are important variables affecting the electrode material's capacitance performance.[22] Conversely, when the activation temperature is increased to 900 °C, the plateau shifts downward and some of the micropore and mesopore structure collapses (Fig. 4a). Thus, the micropore volume decreased to 0.11 $cm^3\ g^{-1}$, and the specific surface area decreased to 1931.77 $m^2\ g^{-1}$.[23] As shown in Fig. 4b, both TG_{1-1}-800 and TG_{1-2}-800 samples exhibit distinct plateaus in the low-pressure range, suggesting that there is a sizable number of micropores present. A type II isotherm with steep adsorption is displayed by the TG_{1-4}-800 sample, where micropores were destroyed by additional activation.[21]

TG_{1-3}-600, TG_{1-3}-700, TG_{1-3}-800, and TG_{1-1}-800 samples have type H4 weak hysteresis loops according to the IUPAC classification of hysteresis loops for desorption isotherms, while TG_{1-2}-800 sample exhibits a transit from type H_4 to H3 hysteresis loops. Furthermore, it is clear that TG_{1-2}-800 sample has an apparent hysteresis loop, indicating inadequate pore openness and a rough pore wall in the absence of sufficient activation of $ZnCl_2$.[24] Although type H4 hysteresis loops are

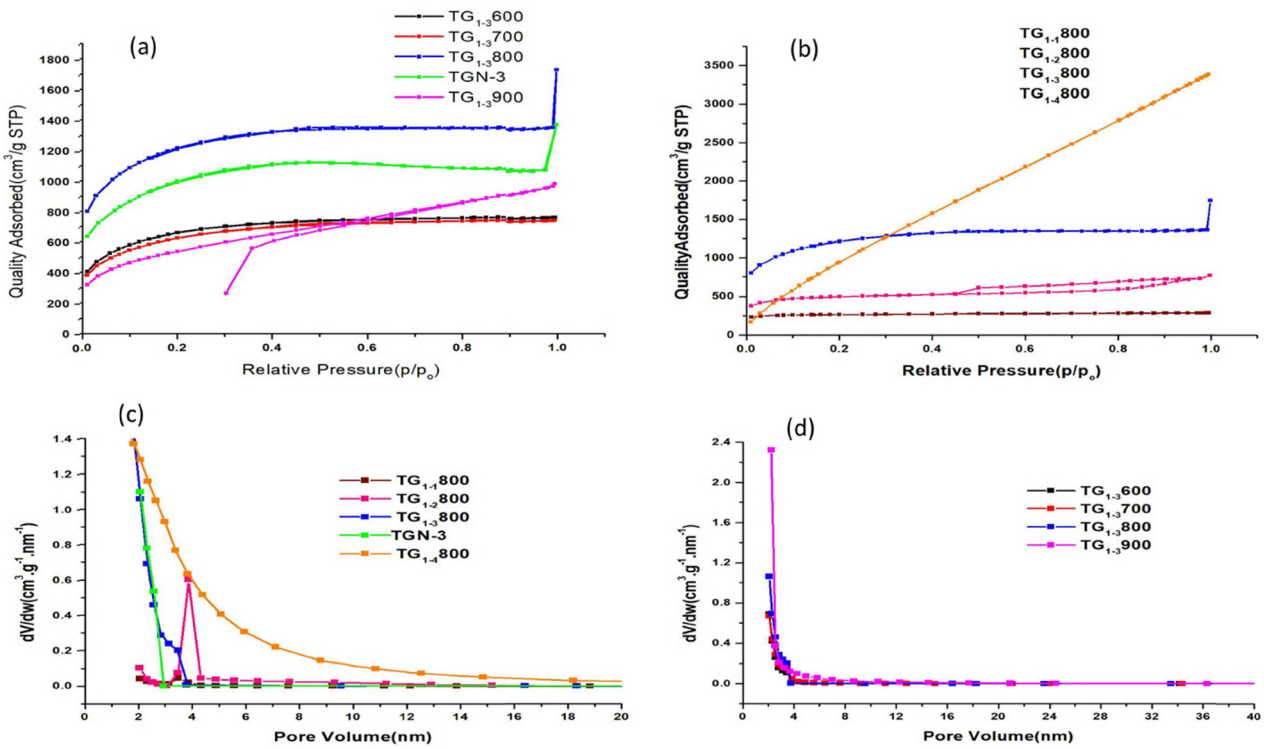

Fig. 4 Adsorption and desorption isotherms of activated TG/$ZnCl_2$ (a) with a 1 : 3 ratio at 600 °C, 700 °C, 800 °C, 900 °C and TGN-3 and (b) with ratios of 1 : 1 to 1 : 4 at 800 °C. (c) Pore size distribution measured forTG_{1-1}-800, TG_{1-2}-800, TG_{1-3}-800, TG_{1-4}-800 and TGN-3 based on N_2 desorption data. (d) Pore size distribution measured forTG_{1-3}-600, TG_{1-3}-700, TG_{1-3}-800 and TG_{1-3}-900 based on N_2 desorption data.

always found in materials with narrow slit-shaped pores that contain both micropores and mesopores, type H3 and H4 hysteresis loops are linked to slit-shaped pores.[25] Using the BJH theory, the pore size distribution (Fig. 4c) was computed from the desorption branch of the isotherm. Table 1 shows how the mass ratio of TG/$ZnCl_2$ affects the textural development of the TG-derived carbon porosity properties at various ratios of 1 : 1, 1 : 2, 1 : 3, and 1 : 4. The growth of porosity, particularly at the mesopore level, is significantly influenced by the activation ratio. As the activation ratio increased, the BET surface area, total pore volume, average pore diameter, and exterior surface area of the TG_n-800 samples exhibited an upward trend until the impregnation ratio reached 1 : 3. Since the impact of $ZnCl_2$ inhibits tar formation and promotes volatile release at low impregnation ratios, more micropores are created. However, a larger impregnation ratio causes the pores to inflate further in the impregnated precursor material and release more volatiles during the carbonisation process. The resulting micropores then become mesopores.[26]

However, the TG_{1-4}-800 sample had no micropore surface area or volume when the activation ratio was adjusted to 1 : 4. This is anticipated since many nearby micropores may collapse or create mesopores and macropores. Thus, the ideal impregnation ratio was determined to be 1 : 3 because the EDLC capacity might be efficiently increased by microporous charge storage.[27]

Fig. 4d displays the range of pore size based on N_2 desorption data in TG_{1-3}-*m* at temperatures ranging from 600 to 900 °C. TG_{1-3}-600 sample through TG_{1-3}-900 sample has specific surface areas of 2365.25, 2236.99, 4302.83, and 1931.77 $m^2\ g^{-1}$, respectively, and total pore volumes of 1.186, 1.156, 2.100, and 1.488 $cm^3\ g^{-1}$, respectively. When the activation temperature was increased to 800 °C, more holes were formed, and the specific surface area increased to 4302.83 $m^2\ g^{-1}$. The creation of some micropores and their linking to generate mesopores caused the micropore volume fraction to decrease to 31.61%. However, a fall in the volume fraction of micropores to 7.39% occurs when the activation temperature increases to 900 °C, resulting in the collapse (or sintering of the small pore walls) of a portion of the micro- and mesopore structures. Consequently, the total pore volume decreases from 2.1 to 1.48 $cm^3\ g^{-1}$, and the specific surface area decreases from 4302.83 to 1931.77 $m^2\ g^{-1}$. It is evident that capacitance increases with specific surface area; consequently, the produced sample exhibits superior chemical performance. Thus, 800 °C is chosen as the ideal carbonization temperature for making activated carbon from the TG biopolymer process. The pore size distribution reveals that the volume of mesopores in the TG_{1-3}-800 and TGN-3 samples increases from 68.38% to 82.45%, and the specific surface area decreases from 4302.83 $m^2\ g^{-1}$ in the TG_{1-3}-800 sample to 3595.77 $m^2\ g^{-1}$ in the TGN-3 sample when the TG sample is doped with nitrogen, as shown in Table 1. The volume fraction of micropores decreases from 31.61% to 17.54%. The initial regular structure is likely to be distorted as a result of the mesopores expanding in a particular direction owing to the increased amount of nitrogen functional groups on the carbon surface.[25] This is confirmed by the XRD diffraction measurements. More active areas for charge storage may be available owing to the severely flawed structure.[28]

The quick filling of small pores with electrolyte is thus made possible by TGN-3, which has a large specific surface area and a more significant pore size. These mesopores serve as conduits for rapid electrolyte transport and diffusion. The TGN-3 electrode active material seems to have a greater specific capacity and rate of operation according to the results of N_2 adsorption–desorption and pore size distribution.[29]

3.5. XRD analysis

The phase structure of the samples was characterized by XRD. The XRD patterns of TG_n-*m*, TGN-3 and TGN-3@Ni materials are shown in Fig. 5. All the patterns exhibited two broad XRD peaks between 22 and 30 and 42 and 45, corresponding to the (002) interlayer spacing between adjacent graphite layers and the (100) in-plane ordering of graphite, respectively.[30]

Remarkably, when the impregnation ratio of the samples in activation with $ZnCl_2$ (Fig. 5a) and the carbonization temperature increased (Fig. 5b), the diffraction peak (002) of the samples decreased significantly and became wider, and at the same time, the intensity of the plane (100) also decreased during the N-doping process of the TGN-3 sample (Fig. 5a), and the carbon network becomes more and more disordered.[20] These points indicate that a large number of amorphous structures are formed owing to the presence of an abundant density of pores in the TGN-3 sample, with a high specific surface area.[31,32]

The diffraction peaks at the (2θ) angles of 37.24, 43.36, 63.0, 75.44, and 79.56, which correspond to the (111), (200), (220), (311), and (222) planes of the cubic NiO, respectively (JCPDS no. 47.1049), provide additional evidence in the presence of NiO and further analysis of the crystal structure of the TGN-3@Ni composite (Fig. 5c). Furthermore, the high crystallinity of the TGN-3@Ni composite is shown by the existence of substantial diffraction peak intensities.[33]

3.6. Raman spectroscopy analysis

To comprehend the structural development of the modified carbon activated at various temperatures, Raman scattering measurements were performed. Raman spectra (Fig. 5d and e) reveal the graphitization quality of the TG_n-*m* materials.

All the TG_n-*m* materials exhibit two characteristic peaks: a D-band (near 1336 C m^{-1}) and a G-band (near 1592 C m^{-1}), representing the disordered and graphitic nature, respectively. The graphitic band is closely associated with the vibrations of sp^2-bonded carbon atoms in the 2d hexagonal lattice, while the defect peak arises owing to sp^3-hybridized carbon.[34]

The intensity ratio of the D to G band (I_D/I_G) can reflect the graphitization degree of carbon materials.[35] The calculated I_D/I_G values of TG_{1-3}-600, TG_{1-3}-700, TG_{1-3}-900, TG_{1-1}-800, TG_{1-2}-800, TG_{1-3}-800, TG_{1-4}-800, and TGN-3 are 0.767, 0.900, 0.936, 0.840, 0.880, 0.866, 0.938, and 0.923, respectively.

The increase in regular carbon content at 800 °C shows that not only are more holes based on SEM and TEM data created

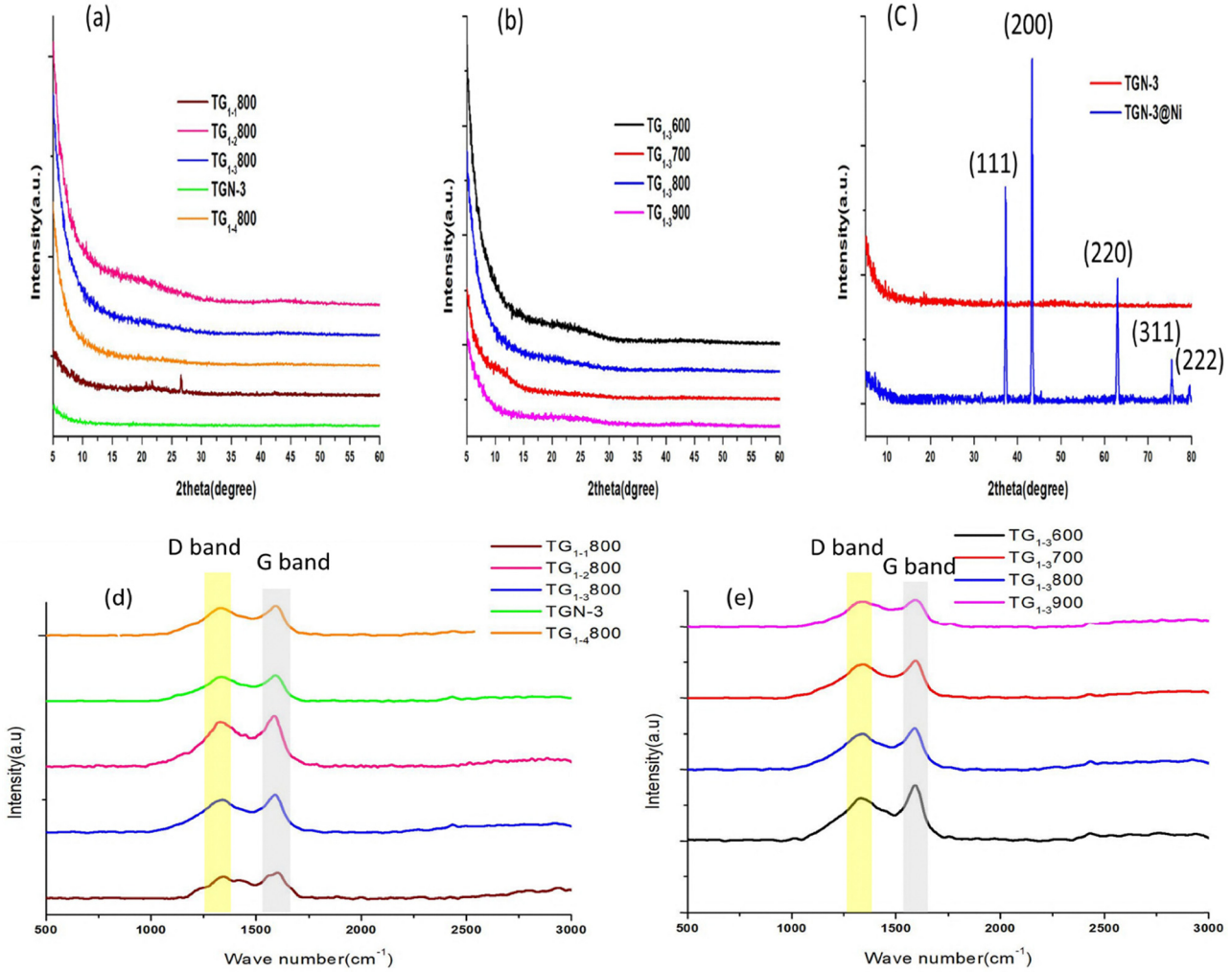

Fig. 5 XRD patterns for activated TG (a) with ratios of 1 : 1 to 1 : 4 and TGN-3 at 800 °C and (b) with a 1 : 3 ratio at 600 °C, 700 °C, 800 °C and 900 °C. XRD pattern of the TGN-3@Ni composite (c). Raman spectra of the activated TG (d) with ratios of 1 : 1 to 1 : 4 and TGN-3 at 800 °C and (e) with a 1 : 3 ratio at 600 °C, 700 °C, 800 °C, and 900 °C.

after the activation process, but also the degree of graphitization increases. The sample activated at 600 °C has the maximum degree of graphitization, but graphitization decreases as the activation temperature increases. Additionally, the results show that N-doping and $ZnCl_2$ activation can provide more structural defects, leading to a higher degree of disorder.[28]

The equivalent series resistance of supercapacitors should decrease as a result of the enhanced electric conductivity caused by the enhanced graphite degree of activated carbon.[36]

3.7. XPS analysis

X-ray photoelectron spectroscopy (XPS) is used to examine the elemental composition, chemical states, and N doping in activated carbon. As shown in Fig. 6a, the survey spectra of the samples contain N, O, C, and Ni atoms.

Fig. 6b shows the XPS spectrum of TGN-3. Three prominent peaks around 285 eV, 400 eV, and 533 eV correspond to the 1s peaks of carbon, nitrogen, and oxygen, respectively. The peak at 285 eV verifies the presence of amorphous carbon.[16]

The TGN-3 sample's high-resolution C 1s spectra (Fig. 6c) identified three peaks: C═C (284.2 eV), C–C/C═N (∼285.2 eV), and O–C═O (288.8 eV).[37–39]

Furthermore, the nitrogen dopant profiles showed two primary peaks at about 400.2 and 398.3 eV (Fig. 6d), corresponding to pyrrolic N (N-5) and pyridinic N (N-6), respectively. Exceptional electron donor capabilities and charge transfer rates created by pyrrolic-N and pyridinic-N might greatly enhance the activity of the electron transfer process.[20] The XPS results indicate that the mass ratio of nitrogen in the treated activated carbon is 1.23%.

The O 1s spectra revealed two peaks with binding energies of 530.1 and 531.8 eV, representing C═O groups (O-I)/Ni–O band and C–OH/C–O–C groups (O-II), respectively.[40]

Fig. 6e shows that TGN-3 has more O-II, which can react with OH^- in an alkaline electrolyte to give pseudocapacitance. Consequently, carbon-based materials containing O- and N-based functional groups might generate reversible faradaic processes and yield pseudocapacitance. These O- and N-based

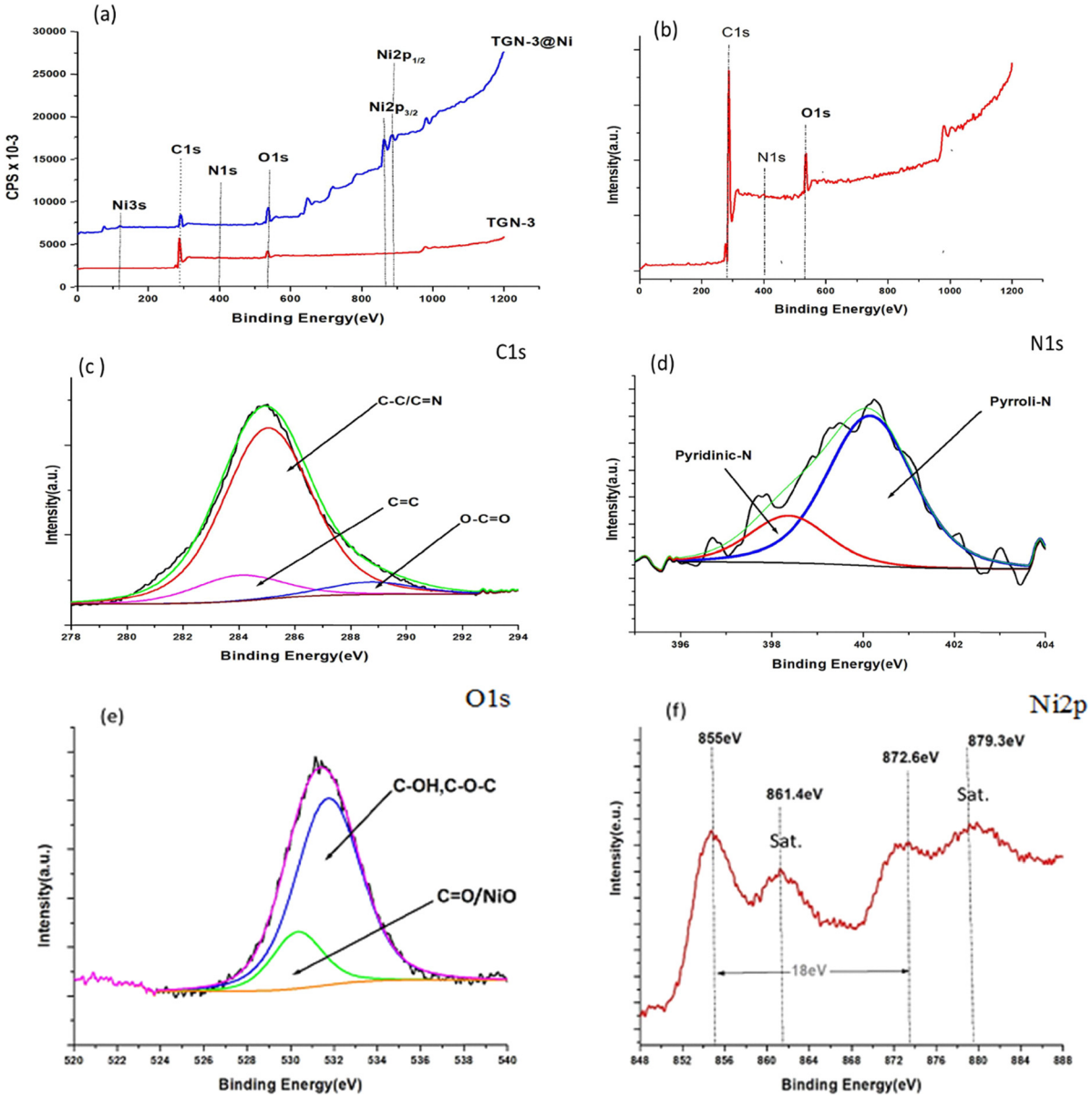

Fig. 6 (a) XPS survey spectra of TGN-3@Ni and TGN-3. XPS spectra of (b) TGN-3, (c) C 1s, (d) N 1s and (e) O 1s. (f) Ni 2p and XPS spectra of composite TGN-3@Ni.

functional groups may also improve the electrical conductivity and wettability of porous carbons.[41]

Ni $2p_{1/2}$ and Ni $2p_{3/2}$ are identified by the peaks in the XPS spectra of Ni 2p (Fig. 6f) centered at 872.6 eV and 855 eV, respectively. Each of these peaks has a shakeup satellite peak at a higher binding energy of about 6.0 eV. A feature of Ni 2p in the NiO of the composite is the spin energy separation between Ni $2p_{1/2}$ and Ni $2p_{3/2}$ peaks, which is approximately 18 eV.[42]

3.8. Electrochemical performance analysis (three-electrode system)

We used a three-electrode setup to analyze all carbon material samples in 6 M KOH electrolytes. The electrochemical behavior of the carbons was estimated using cyclic voltammetry (CV). CV curves of TG_{1-3}-600, TG_{1-3}-700, TG_{1-3}-800, and TG_{1-3}-900 measured at a scan rate of 50 mV s^{-1} are shown in Fig. 7a.

TG_{1-1}-800, TG_{1-2}-800, TG_{1-3}-800, and TG_{1-4}-800 activation CV curves at various ratios with $ZnCl_2$ in a scan rate of 50 mV s^{-1} are shown in Fig. 7b, while Fig. 7c displays the TGN-1, TGN-2, TGN-3, and TGN-4 CV curves with respect to various N-doping ratios in the voltage ranging from −1.18 to 0.2 V measured at a scanning speed of 50 mV s^{-1}.

The CV curves of these porous materials showed rectangular forms with a small distortion, as shown in Fig. 7a and b. This behavior was characteristic of an almost perfect EDLC based on ionic adsorption and desorption. The nearly rectangular CV curves in Fig. 7c also showed that these carbon materials, which are porous as electrode materials, had good, rapid

charge and discharge features. However, the double-layer and faradaic (pseudocapacitive) charge storage mechanisms between the active materials and electrolytes, which were induced by nitrogenous groups, overlapped, slightly distorting the CV curves.[43,44]

In contrast to the EDLC mechanism, pseudocapacitive behavior is typically accompanied by a high specific capacitance and a comparatively high energy density. This is because, in contrast to EDLC, where ion adsorption occurs only at the surface layers, the bulk of the material is exposed to redox processes.[45]

The material's specific capacitance is reflected in the cyclic voltammetric area. Because of its high specific surface area (up to 3595.77 $m^2\ g^{-1}$) and suitable nitrogen concentration (1.23%), the TGN-3 sample had the largest CV curve area when compared to other samples, confirming that it had the highest specific capacitance (Table 2).[43]

Fig. 7d displays sample TGN-3's CV curve at various scan rates ranging from 10 to 200 mV s^{-1}. The area of the CV curves grows steadily as the sweep speed increases while maintaining a nearly constant shape, suggesting that the TGN-3 material possesses superior charge propagation and quick ion transport.[35]

The specific gravimetric capacitances (C, F g^{-1}) were calculated from the CV curves according to eqn (2):

$$C = \frac{A}{2v\Delta V m'} \quad (2)$$

where A is the area under the CV curve (mA V), v is the scan rate (mV s^{-1}), ΔV is the potential window (V) and m is the mass of the working electrode (g).[46]

Table 2 shows the specific capacitance data of these electrodes. These values are smaller than the value reported for TGN-3.

The study mentioned above shows that TGN-3 has high specific capacitances and good rate capability, which are mostly due to the following factors:

(1) N-atom doping, such as N-6 and N-5 doping, effectively provides the Faraday effect to improve the performance of supercapacitors;[47] (2) the generation of pseudocapacitance can increase the capacity of the capacitor through the attraction of the N atom in the carbon material; and (3) the charge storage within microporosity is strengthened by the abundance of active sites that are generated *in situ* at the pores of nitrogen-doped porous carbons with permeable defect-related porosity, which can quickly contact the electrolyte and increase the capacity of the double-layer capacitor.[29]

Galvanostatic charge–discharge (GCD) tests were conducted across a potential ranging from −1.02 to 0.2 V to validate the electrochemical characteristics of TGN-3. The GCD curves recorded at different applied currents of 1, 2, and 5 A g^{-1} are displayed in Fig. 7e. Additionally, because the electrolyte ions have enough time to enter and diffuse into the porosity at lower current densities, the charge–discharge time significantly lowers as the current density increases. In other words, the TGN-3 sample shows the maximum charge–discharge duration at a current density of 1 A g^{-1}.

Similar to the CV curve data, the GCD results confirm that the TGN-3 sample has the best capacitive performance and exhibits capacitive behavior. TGN-3@Ni composite was created in this work using a hydrothermal process and calcination. XPS, XRD and TEM results showed that the precursor (TGN-3) had successfully transformed into TGN-3@Ni. TGN-3@Ni's electrochemical performance was initially assessed using a three-electrode setup in a 6 M KOH solution. The TGN-3@Ni electrode's CV curves at various scan rates are displayed in Fig. 7f. The TGN-3@Ni electrode exhibits advantageous pseudocapacitive behavior with reversible faradaic charge storage, as evidenced by the integral area of the CV curves growing larger and the shape remaining constant as the scan rate increases.[33]

The CV curves showed a distinct pair of redox peaks, one of which is anodic during the oxidation reaction of Ni^{2+} to Ni^{3+} and the other is cathodic during the reverse process. This suggests that the faradaic reaction is primarily responsible for capacitance properties.[48]

$$NiO + OH^- \leftrightarrow NiOOH + e^-$$

Owing to an increase in internal diffusion resistance within the electrode active material, the current increased as the scan rate increased, causing the oxidation peaks to shift to a more positive position and the reduction peaks to shift to a more negative position.[49]

As shown in Fig. 7g, the capacitance property was determined using galvanostatic charge–discharge throughout a potential range of 0–0.5 V as the current density increased from 1 to 40 A g^{-1}. All GCD curves had symmetrical forms, indicating a reversible redox reaction of the TGN-3@Ni electrode with notable pseudocapacitance performance.[33,41] The specific capacitance of a single electrode (C_s, F g^{-1}) for the three-electrode system was calculated from the discharge curves according to the following equation:[50]

$$C_S = \frac{I \cdot \Delta t}{m \cdot \Delta V}, \quad (3)$$

where I is the discharge current (A), Δt (s) is the discharge time, m (g) is the mass of the active material of the individual electrode, and ΔV (V) is the voltage range.

Specific capacitances of the TGN-3@Ni electrode material were measured using the discharge curves 319.5, 292.4, 260.8, 237, and 215 F g^{-1} at 5, 10, 20, 30, and 40 A g^{-1}, respectively.

Furthermore, increasing the current density to 40 A g^{-1} resulted in 67.2% of the original capacity remaining. Capacitance retention at such high current density is due to the advantages of the TGN-3@Ni composite. This might be ascribed to the large specific surface area and higher conductivity of Tragacanth-derived porous carbon containing NiO and N. The large surface area of porous carbon allows for large numbers of superficial electroactive species to participate in faradaic redox reactions. Furthermore, the active material's enhanced conductivity creates a conduit for electron transport, allowing for faster charging and discharging. Consequently,

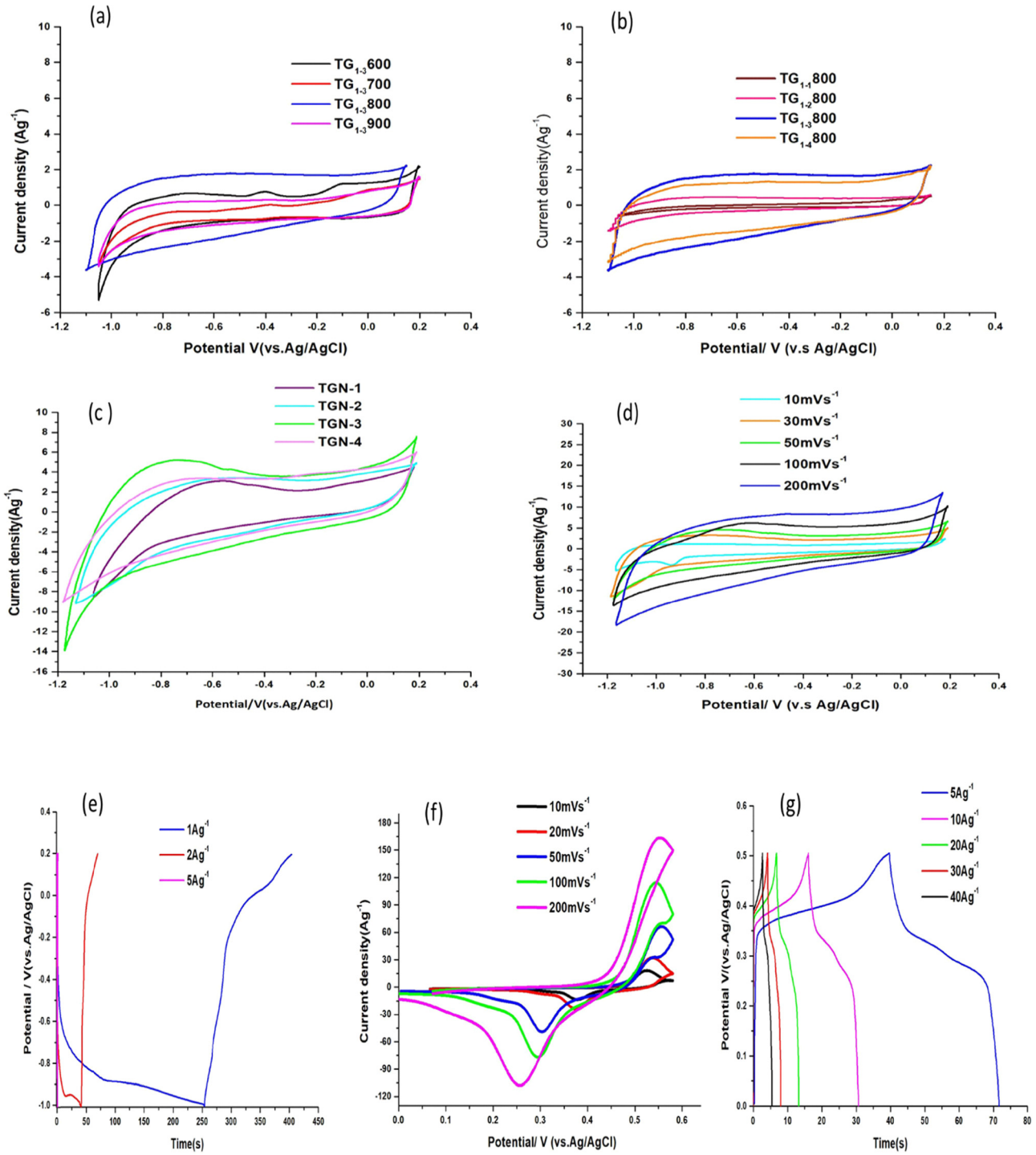

Fig. 7 (a) Comparison of CV curves for TG_{1-3}-600, TG_{1-3}-700, TG_{1-3}-800 and TG_{1-3}-900 measured at a scan rate of 50 mV s^{-1}. (b) Comparison of CV curves for TG_{1-1}-800, TG_{1-2}-800, TG_{1-3}-800, and TG_{1-4}-800 measured at a scan rate of 50 mV s^{-1}. (c) Comparison of CV curves for TGN-1, TGN-2, TGN-3, and TGN-4 measured at a scan rate of 50 mV s^{-1}. (d) CV curves of TGN-3 at different scan rates. (e) Charge–discharge curves of TGN-3 at different current densities. (f) CV curves of TGN-3 @Ni at different scan rates. (g) Charge–discharge curves of TGN-3 @Ni at different current densities.

integrating these two materials into a single electrode enhanced the electrochemical characteristics of supercapacitor applications.[40]

This study's electrochemical results are compared to prior recent findings on NiO/carbon with diverse configurations, as shown in Table 3.

The high specific capacitance of the TGN-3 @Ni nanocomposite is superior to or comparable to most of the recently reported NiO-based electrode materials. Given the above, the as-prepared TGN-3@Ni, which has outstanding electrochemical characteristics, is a viable choice for the positive electrode active material in supercapacitors.

Table 2 Specific capacitance (F g^{-1}). Electrode carbon material at a scan rate of 50 (mV s^{-1})

Electrode material	Specific capacitance (F g^{-1}) at a scan rate of 50 (mV s^{-1})
TG_{1-1}-800	1.87
TG_{1-2}-800	6.55
TG_{1-3}-800	27.83
TG_{1-3}-600	15.94
TG_{1-3}-700	7.75
TG_{1-3}-900	12.27
TG_{1-4}-800	21.18
TGN-1	32.17
TGN-2	46.38
TGN-3	79.57
TGN-4	51.52

The EIS test was performed to evaluate the transport kinetics for the electrochemical reaction process.[42] Each impedance spectrum consists of three main components: intrinsic ohmic resistance (R_s), interfacial charge transfer resistance (R_{ct}), and Warburg diffusion resistance (R_w). R_s varies slightly with current density. In contrast, R_{ct} and R_w are related to ion diffusion in the electrolyte or at the electrolyte–electrode interface and are therefore sensitive to the shape and quality of the current density surface associated with the electrode and ion migration.[57,58]

The Nyquist plots of the carbon samples, which are fitted by an equivalent circuit used at different temperatures, are plotted in the support section (Fig. S2). The TG_{1-3}-600, TG_{1-3}-700, TG_{1-3}-800 and TG_{1-3}-900 electrodes had R_s values of 0.43, 0.47, 0.47 and 0.43 Ω, and charge transfer resistances of 2991, 5759, 296.8 and 1686 Ω, respectively. These findings suggest that the electrode resistance (R_{ct}) is decreased by activation at 800 °C.

The disparity between the pore size distribution and the surface area difference in the carbon samples may be because the R_{ct} for TG_{1-3}-800 in the high frequency region of this fitting was lower than the R_{ct} for TG_{1-3}-600, TG_{1-3}-700 and TG_{1-3}-900. Furthermore, the carbon-containing electrode's TG_{1-3}-800 mesoporous shape makes the pores more accessible. The straight line slope of the TG_{1-3}-800 sample is sharper in the low frequency region, which could be because larger pores are more accessible than smaller ones at 800 °C.[59] TGN-3's R_{ct} (2.5 Ω) is substantially lower than TG_{1-3}-800's R_{ct} (296.8 Ω). This suggests that doping activated carbon with heteroatoms lowers the R_{ct}. This finding suggests that electron conductivity is enhanced when functions containing nitrogen are added to the carbon matrix (Fig. S3). Remarkably, when doped with different ratios, the ratio of 1 : 3, or TGN-3, has a lower Warburg resistance in the mid-frequency zone and a smaller R_{ct} in the high-frequency region. At low frequencies, the slope of the straight line is steeper. This suggests that activated carbon doped with nitrogen (TGN-3) has the diffusion resistance of the electrode material, which is smaller and closer to the ideal capacitance behavior.[14,60,61]

However, TGN-4's electronic conductivity decreases in comparison to TGN-3's due to an excess of defect sites in the conductive carbon framework caused by the overdose of urea (Fig. 8a).[62]

Fig. 8b compares the Nyquist plots of impedance spectra for TGN-3 and TGN-3@Ni. The small R_{ct} in the high-frequency region indicates the presence of a large pore structure, particularly for mesopores and macropores, which have more pore accessibility than micropores.[63] The R_{ct} values for TGN-3 and TGN-3@Ni were predicted to be 2.54 Ω and 5.57 Ω, respectively, with R_s values of about 0.32 Ω and 0.3 Ω, respectively. A lower R_s value often indicates greater electrical conductivity. Apart from the effect of large pores, the inclusion of nickel oxide nanoparticles in TGN-3@Ni can assist in boosting the conductivity of the carbon matrix.[63] The TGN-3 sample exhibits a tiny semicircle in the high-frequency area before transitioning to linearity in the low-frequency range. This shows that the electrode material's diffusion resistance is lower and closer to the optimum capacitance behaviour.

3.9. Electrochemical properties of the TGN-3@Ni//TGN-3 ASC device

To examine the practical use of TGN-3@Ni and TGN-3 electrodes, an asymmetric device is fabricated by pairing TGN-3@Ni and TGN-3 as the cathode and anode, respectively. With a

Table 3 Comparison of the present work with the literature on NiO/carbon composites

Electrode material	Specific capacitance (F g^{-1})	Potential window (V *vs.* ref. electrode)	Rate capability in % retention (current density range)	Stability in % retention (number of cycles)	Electrolyte	Ref.
NiO@SW-CFs	356 at 2 A g^{-1}	0.1–0.6 (V *vs.* Hg/HgO)	40% (2–30 A g^{-1})	93%, 10 A g^{-1} (5000 cycles)	2 M KOH	51
NiO@AMCRs	858 at 3 A g^{-1}	0–0.45 (V *vs.* SCE)	54% (3–50 A g^{-1})	66%, 10 A g^{-1} (10 000 cycles)	2 MKOH	51
CNF/NiO	674 at 0.5 A g^{-1}	0–0.6 (V *vs.* Hg/HgO)	63% (0.5–10 A g^{-1})	98.6%, 0.5 A g^{-1} (5000 cycles)	6 M KOH	20
NiO/NCHS composite	585 at 1 A g^{-1}	0–0.5 (V *vs.* Ag/AgCl)	50.4% (1–10 A g^{-1})	115%, 5 A g^{-1} (6000 cycles)	2 M KOH	42
NC/Ni@NiO	390 at 2 A g^{-1}	0–0.4 (V *vs.* SCE)	59.4% (1–10 A g^{-1})	70.2%, 2 A g^{-1} (5000 cycle)	6 M KOH	52
3D flower-like nickel oxide/nickel composites	363.7 at 0.5 A g^{-1}	0–0.5 (V *vs.* Hg/HgO)	63.7% (1–8 A g^{-1})	89%, 1 A g^{-1} (1000 cycles)	6 M KOH	53
NSCDC/NiO	804 at 1 A g^{-1}	−0.4 to 0.8 V	53.48% (1–10 A g^{-1})	73.2%, 5 A g^{-1} (5000 cycles)	3 M KOH	54
SDCC-NiO	23.25 at 1 A g^{-1}	—	36.68% (5–15 A g^{-1})	—	1 M KOH	46
PC-NiO	811.46 at 1 A g^{-1}	0–0.6 (V *vs.* SCE)	—	95.25%, 1 A g^{-1} (1000 cycles)	6 M KOH	55
Ce/Ni composite	268 at 0.2 A g^{-1}	0–0.5 (V *vs.* Ag/AgCl)	74.2% (0.2–2 A g^{-1})	97%, 0.2 A g^{-1} (2000 cycles)	6 M KOH	56
TGN-3@Ni	319.5 at 5 A g^{-1}	−1.0 to 0 (V *vs.* SCE)	67.29% (5–40 A g^{-1})	96.12%, 5 A g^{-1} 8000 cycles (ASC)	6 M KOH	This work
		0–0.5 (V *vs.* Ag/AgCl)				

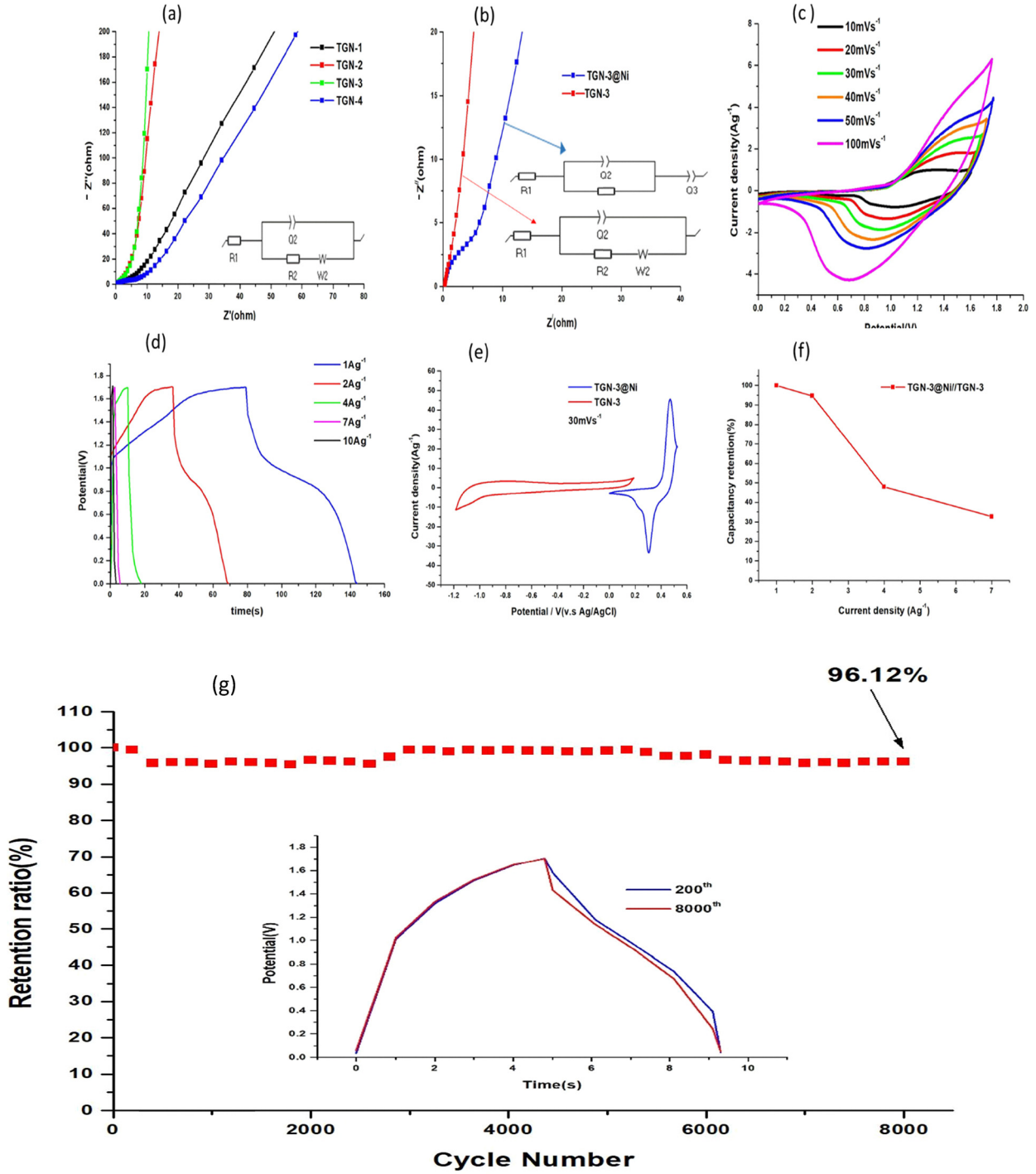

Fig. 8 (a) Comparison of Nyquist plots for TGN-1, TGN-2, TGN-3 and TGN-4 with a frequency ranging from 0.01 Hz to 100 kHz. (b) Nyquist plots for TGN-3 and TGN-3@Ni. (c) The CV curves of TGN-3@Ni//TGN-3 asymmetric supercapacitor device at different sweep rates in a 6 M KOH electrolyte. (d) GCD curves of the assembled device at different current densities. (e) Comparative CV curves of TGN-3 and TGN-3@Ni tested in a three-electrode configuration at 30 mV s^{-1}. (f) Gravimetric capacitance retention of the TGN-3@Ni//TGN-3 device as a function of the applied current density. (g) Changes in the capacitance retention of the TGN-3@Ni//TGN-3 ASC as a function of cycle number.

potential window of 1.7 V, CV plots of the built TGN-3@Ni//TGN-3 device at several sweep speeds ranging from 10 to 100 mV s^{-1} are shown in Fig. 8c. Because of the fast transport of electrons and diffusion of ions, the CV curves of the TGN-3@Ni//TGN-3 device show a large current response while maintaining their primary shape with regard to the excellent rate capability and reversibility, confirming an efficient charge storage behavior. To further assess electrochemical performance,

GCD measurements were performed at current densities ranging from 1 A g^{-1} to 10 A g^{-1}, as shown in Fig. 8d. Each discharge line reveals that capacitance is mostly produced from plateaus from the faradaic process, which is consistent with the results of CV testing. The shape of GCD curves retain nearly symmetrical plateaus, confirming the ASC's consistent capacitive performance.[16,53] For the asymmetric supercapacitor, the mass-specific capacitance is calculated using the following equation:[64]

$$C_{ASC} = \frac{I \cdot \Delta t}{M \cdot \Delta V}, \quad (4)$$

where M (g) denotes the total mass of the active substances on the two electrodes.

The specific energy (E, Wh kg^{-1}) and power (P, W kg^{-1}) were determined consistently with the galvanostatic data using the following equations:

$$E = \frac{1}{2} C_{ASC} \Delta V^2 \times \frac{1}{3.6}, \quad (5)$$

$$P = 3600 \frac{E}{\Delta t}, \quad (6)$$

where ΔV (V) is the cell voltage for charging and discharging.[50] Fig. 8e compares the CV curves of TGN-3@Ni and TGN-3 electrode materials evaluated in a three-electrode setup at a scan rate of 30 mV s^{-1}.

The TGN-3@Ni electrode has a potential window of 0 to 0.56 V, while the TGN-3 electrode has a potential window of −1.18 to 0.2 V. Thus, an operating voltage of 1.74 V is predicted from an ASC with the TGN-3@Ni as the positive electrode and the TGN-3 as the negative electrode because the total two-electrode cell voltage is the sum of the potentials of the positive and negative electrodes.[65]

The specific gravimetric capacitance of the asymmetric supercapacitor decreased with a fourfold increase in discharge current density (with 47.94% capacitance retention) because diffusion at high current densities impeded the migration of ions and OH^- in the electrode, resulting in low electrochemical utilization of electroactive materials (Fig. 8f).[66]

Cyclic stability is an important feature of supercapacitors. As a result, the cycle stability of the TGN-3@Ni//TGN-3 device was studied by charging and discharging at 5 A g^{-1}, as depicted in Fig. 8g. The specific capacitance of the TGN-3@Ni//TGN-3 device decreases somewhat after 8000 cycles, but it retains 96.12% of its initial value, indicating outstanding recyclability. These results indicate that choosing an appropriate strategy, including optimizing the carbon pore structure, incorporating heteroatoms, and combining carbon materials with metal oxides, is an effective strategy to significantly enhance their performance as supercapacitor electrode materials.[67,68]

4. Conclusions

In summary, we successfully prepared a porous activated carbon doped with nitrogen derived from tragacanth gum at an optimized temperature of 800 °C and an optimal 1 : 3 saturation ratio with $ZnCl_2$ as the activating agent and doped 1 : 3 with urea as the nitrogen source using a simple method for the first time. The resulting TGN-3 sample has a nitrogen content of 1.23% and a high specific surface area of 3595.77 m^2 g^{-1}. Additionally, the CV curve data and GCD results confirmed that the TGN-3 sample exhibited the best capacitive performance and capacitive behavior. Then, NiO nanoparticles were embedded in the TGN-3 carbon matrix using a hydrothermal method and a calcination process. This situation further reduces the internal and interfacial resistance of the matrix. The synergistic effect of these features in the TGN-3@Ni composite causes it to exhibit good electrical conductivity and excellent electrochemical performance. In a three-electrode setup, this electrode provides a specific capacity of 319.5 F g^{-1} at a current density of 5 A g^{-1}. In the same system, the TGN-3 electrode's specific capacity is 124.78 F g^{-1} at a current density of 1 A g^{-1}, and the as-assembled TGN-3@Ni//TGN-3 may function at a stable electrochemical window up to 1.7 V and provide a high specific capacity of 40.06 F g^{-1}. At a power density of 881.07 W kg^{-1}, it can also provide a high energy density of 16.07 Wh kg^{-1}. According to these findings, the TGN-3@Ni composite shows promise as an electrode material for energy storage applications. Remarkably, other metals and metal oxides can also be tested in order to enhance the conductivity of TGN-3 and give a better performance to the end composite. Therefore, more studies should be conducted in this field in the near future.

Conflicts of interest

There are no conflicts to declare.

Data availability

The datasets supporting this article have been included as part of the SI. See DOI: **https://doi.org/10.1039/d5ma00328h**.

Acknowledgements

The authors would like to acknowledge the Iran University of Science & Technology and Shahed University for sponsoring this work.

References

1 S. Ahmad, M. Ahmad, K. Manzoor, R. Purwar and S. Ikram, *Int. J. Biol. Macromol.*, 2019, **136**, 870–890.
2 S. Tang, L. Jiang, Z. Jiang, Y. Ma, Y. Zhang and S. Su, *Polymers*, 2023, **15**, 2942.
3 E. N. Zare, P. Makvandi and F. R. Tay, *Carbohydr. Polym.*, 2019, **212**, 450–467.
4 A. Scalia, P. Zaccagnini, M. Armandi, G. Latini, D. Versaci, V. Lanzio, A. Varzi, S. Passerini and A. Lamberti, *ChemSusChem*, 2021, **14**, 356–362.

5 Y. Lu, H. Zhou, W. Zhao, J. Jiang, J. Du and L. Zhao, *Int. J. Biol. Macromol.*, 2024, **282**, 137299.
6 M. Darroudi, Z. Sabouri, R. K. Oskuee, A. K. Zak, H. Kargar and M. H. N. Abd Hamid, *Ceram. Int.*, 2013, **39**, 9195–9199.
7 S. Taghavi Fardood, A. Ramazani and S. Joo, *J. Struct. Chem.*, 2018, **59**, 482–486.
8 M. K. Indana, B. R. Gangapuram, R. Dadigala, R. Bandi and V. Guttena, *J. Anal. Sci. Technol.*, 2016, **7**, 19.
9 S. Mallakpour and M. Okhovat, *Int. J. Biol. Macromol.*, 2021, **175**, 330–340.
10 Z. Guo, X. Han, C. Zhang, S. He, K. Liu, J. Hu, W. Yang, S. Jian, S. Jiang and G. Duan, *Chin. Chem. Lett.*, 2024, **35**, 109007.
11 B. Chang, Y. Wang, K. Pei, S. Yang and X. Dong, *RSC Adv.*, 2014, **4**, 40546–40552.
12 S. Sangon, K. Kotebantao, T. Suyala, Y. Ngernyen, A. J. Hunt and N. Supanchaiyamat, *Environ. Sci.: Water Res. Technol.*, 2024, **10**, 1389–1405.
13 J. Su, Y. Xu, R. Yang, X. Lin, Y. Xie, H. Zhao, C. Shi, X. Dong, C. Wang and Y. Qing, *Colloids Surf., A*, 2024, **701**, 134964.
14 J. Chen, Y. Lin, J. Liu, D. Wu, X. Bai, D. Chen and H. Li, *J. Energy Storage*, 2021, **39**, 102640.
15 A. Querejeta-Fernandez, M. Parras, A. Varela, F. del Monte, M. Garcia-Hernandez and J. M. Gonzalez-Calbet, *Chem. Mater.*, 2010, **22**, 6529–6541.
16 Y. Chen, R. Hu, J. Qi, Y. Sui, Y. He, Q. Meng, F. Wei and Y. Ren, *Mater. Res. Express*, 2019, **6**, 095605.
17 H. Chen, H. Wei, N. Fu, W. Qian, Y. Liu, H. Lin and S. Han, *J. Mater. Sci.*, 2018, **53**, 2669–2684.
18 L. Ma, G. Sun, J. Ran, S. Lv, X. Shen and H. Tong, *ACS Appl. Mater. Interfaces*, 2018, **10**, 22278–22290.
19 X. Jiang, S. Deng, J. Liu, N. Qi and Z. Chen, *J. Energy Storage*, 2021, **37**, 102426.
20 L. Sun, Y. Sun, Q. Fu and C. Pan, *J. Alloys Compd.*, 2021, **888**, 161488.
21 L. Peng, Y. Liang, H. Dong, H. Hu, X. Zhao, Y. Cai, Y. Xiao, Y. Liu and M. Zheng, *J. Power Sources*, 2018, **377**, 151–160.
22 S. Liu, Y. Zhao, B. Zhang, H. Xia, J. Zhou, W. Xie and H. Li, *J. Power Sources*, 2018, **381**, 116–126.
23 Y. Yuan, R. Yi, Y. Sun, J. Zeng, J. Li, J. Hu, Y. Zhao, W. Sun, C. Zhao and L. Yang, *J. Nanomater.*, 2018, **2018**, 7539509.
24 Y. Li, G. Wang, T. Wei, Z. Fan and P. Yan, *Nano Energy*, 2016, **19**, 165–175.
25 Y. Hu, H. Liu, Q. Ke and J. Wang, *J. Mater. Chem. A*, 2014, **2**, 11753–11758.
26 H. Sayğılı and F. Güzel, *J. Cleaner Prod.*, 2016, **113**, 995–1004.
27 M. M. Baig, I. H. Gul, S. M. Baig and F. Shahzad, *J. Energy Storage*, 2021, **44**, 103370.
28 Y. Cui, H. Wang, X. Xu, Y. Lv, J. Shi, W. Liu, S. Chen and X. Wang, *Sustainable Energy Fuels*, 2018, **2**, 381–391.
29 P. Li, C. Yang, C. Wu, Y. Wei, B. Jiang, Y. Jin and W. Wu, *Nanomaterials*, 2022, **12**, 2931.
30 I. Alali, A. U. Shehu and R. Mokaya, *Energy Environ. Sci.*, 2024, **17**, 5024–5038.
31 J. Hou, K. Jiang, M. Tahir, X. Wu, F. Idrees, M. Shen and C. Cao, *J. Power Sources*, 2017, **371**, 148–155.
32 X. Wang, S. Yun, W. Fang, C. Zhang, X. Liang, Z. Lei and Z. Liu, *ACS Sustainable Chem. Eng.*, 2018, **6**, 11397–11407.
33 C. Zhang, F. Cui, Q. Ma and T. Cui, *J. Energy Storage*, 2024, **102**, 114150.
34 P. R. Kasturi, H. Ramasamy, D. Meyrick, Y. S. Lee and R. K. Selvan, *J. Colloid Interface Sci.*, 2019, **554**, 142–156.
35 Y. Lin, Z. Chen, C. Yu and W. Zhong, *Electrochim. Acta*, 2020, **334**, 135615.
36 P. Hao, Z. Zhao, J. Tian, H. Li, Y. Sang, G. Yu, H. Cai, H. Liu, C. Wong and A. Umar, *Nanoscale*, 2014, **6**, 12120–12129.
37 S. Ratso, I. Kruusenberg, M. Vikkisk, U. Joost, E. Shulga, I. Kink, T. Kallio and K. Tammeveski, *Carbon*, 2014, **73**, 361–370.
38 K. Zheng, Y. Li, M. Zhu, X. Yu, M. Zhang, L. Shi and J. Cheng, *J. Power Sources*, 2017, **366**, 270–277.
39 K. Wang, M. Xu, X. Wang, Z. Gu, Q. H. Fan, W. Gibbons and J. Croat, *RSC Adv.*, 2017, **7**, 8236–8240.
40 S. C. Kishore, R. Atchudan, T. N. Jebakumar Immanuel Edison, S. Perumal, M. Alagan, R. Vinodh, M. Shanmugam and Y. R. Lee, *Energy Fuels*, 2020, **34**, 14958–14967.
41 Y. Liu, X. Wang, X. Jiang, X. Li and L. Yu, *Nanoscale*, 2018, **10**, 22848–22860.
42 T. Liu, C. Jiang, B. Cheng, W. You and J. Yu, *J. Power Sources*, 2017, **359**, 371–378.
43 H. Chen, H. Wei, N. Fu, W. Qian, Y. Liu, H. Lin and S. Han, *J. Mater. Sci.*, 2018, **53**, 2669–2684.
44 A. Noori, M. F. El-Kady, M. S. Rahmanifar, R. B. Kaner and M. F. Mousavi, *Chem. Soc. Rev.*, 2019, **48**, 1272–1341.
45 N. Choudhary, C. Li, J. Moore, N. Nagaiah, L. Zhai, Y. Jung and J. Thomas, *Adv. Mater.*, 2017, **29**, 1605336.
46 R. Kumar, A. Soam and V. Sahajwalla, *Mater. Adv.*, 2020, **1**, 609–616.
47 C. Liu, Y. Hou, Y. Li and H. Xiao, *J. Colloid Interface Sci.*, 2022, **614**, 566–573.
48 B. P. Bastakoti, H.-S. Huang, L.-C. Chen, K. C.-W. Wu and Y. Yamauchi, *Chem. Commun.*, 2012, **48**, 9150–9152.
49 J. Ji, L. L. Zhang, H. Ji, Y. Li, X. Zhao, X. Bai, X. Fan, F. Zhang and R. S. Ruoff, *ACS Nano*, 2013, **7**, 6237–6243.
50 X. Li, J. Shen, W. Sun, X. Hong, R. Wang, X. Zhao and X. Yan, *J. Mater. Chem. A*, 2015, **3**, 13244–13253.
51 J. G. Ruiz-Montoya, L. V. Quispe-Garrido, J. C. Gómez, A. M. Baena-Moncada and J. M. Gonçalves, *Sustainable Energy Fuels*, 2021, **5**, 5332–5365.
52 Y. Li, Q. Wei, R. Wang, J. Zhao, Z. Quan, T. Zhan, D. Li, J. Xu, H. Teng and W. Hou, *J. Colloid Interface Sci.*, 2020, **570**, 286–299.
53 X. Liu and F. Liu, *Eur. J. Inorg. Chem.*, 2018, 987–991.
54 J. Pan, W. Zhong, Z. Gao, X. Yang, Y. Zhang, Y. Guan and X. Yan, *Ceram. Int.*, 2021, **47**, 27833–27842.
55 S. A. Al Kiey and M. S. Hasanin, *Environ. Sci. Pollut. Res.*, 2021, **28**, 66888–66900.
56 X. Zhao, H. Chen, S. Wang, Q. Wu, N. Xia and F. Kong, *Mater. Chem. Phys.*, 2018, **215**, 157–162.

57 J. Zhao, Y. Jiang, H. Fan, M. Liu, O. Zhuo, X. Wang, Q. Wu, L. Yang, Y. Ma and Z. Hu, *Adv. Mater.*, 2017, **29**, 1604569.
58 R. Ullah, N. Khan, R. Khattak, M. Khan, M. S. Khan and O. M. Ali, *Polymers*, 2022, **14**, 242.
59 J. Gamby, P. Taberna, P. Simon, J. Fauvarque and M. Chesneau, *J. Power Sources*, 2001, **101**, 109–116.
60 L. Sun, L. Wang, C. Tian, T. Tan, Y. Xie, K. Shi, M. Li and H. Fu, *RSC Adv.*, 2012, **2**, 4498–4506.
61 M. Y. Perdana, B. A. Johan, M. Abdallah, M. E. Hossain, M. A. Aziz, T. N. Baroud and Q. A. Drmosh, *Chem. Rec.*, 2024, **24**, e202400007.
62 M. Chen, T. Le, Y. Zhou, F. Kang and Y. Yang, *ACS Appl. Energy Mater.*, 2020, **3**, 1653–1664.
63 Y. Hui, Y. Shewen, W. Yunfeng, Z. Jiaming, J. Jingwen, C. Jiahao, Z. Qinqin and L. Tongxiang, *J. Alloys Compd.*, 2019, **792**, 976–982.
64 W. Hong, L. Wang, K. Liu, X. Han, Y. Zhou, P. Gao, R. Ding and E. Liu, *J. Alloys Compd.*, 2018, **746**, 292–300.
65 H. Peng, C. Wei, K. Wang, T. Meng, G. Ma, Z. Lei and X. Gong, *ACS Appl. Mater. Interfaces*, 2017, **9**, 17067–17075.
66 Z. Gao, W. Yang, J. Wang, N. Song and X. Li, *Nano Energy*, 2015, **13**, 306–317.
67 L. Wang, S. Chen, L. N. Bengoa, R. M. Gonzalez-Gil and P. Gomez-Romero, *Electrochim. Acta*, 2025, 146722.
68 X. Zhu, Y. Zeng, X. Zhao, D. Liu, W. Lei and S. Lu, *EcoEnergy*, 2025, e70000.